HHS Public Access

Author manuscript

*Nat Biomed Eng*. Author manuscript; available in PMC 2020 December 15.

Published in final edited form as:

*Nat Biomed Eng*. 2020 August ; 4(8): 835–844. doi:10.1038/s41551-020-0570-5.

# Whole-body tracking of single cells via positron emission tomography

**Kyung Oh Jung**[1], **Tae Jin Kim**[1], **Jung Ho Yu**[2], **Siyeon Rhee**[3], **Wei Zhao**[1], **Byunghang Ha**[1], **Kristy Red-Horse**[3], **Sanjiv Sam Gambhir**[2], **Guillem Pratx**[1,*]

[1]Department of Radiation Oncology, Stanford University School of Medicine, Stanford, CA, 94305, USA

[2]Department of Radiology, Stanford University School of Medicine, Stanford, CA, 94305, USA

[3]Department of Biology, Stanford University School of Medicine, Stanford, CA, 94305, USA

## Abstract

In vivo molecular imaging can measure the average kinetics and movement routes of injected cells through the body. Yet owing to the non-specific accumulation of the contrast agent and its efflux from the cells, most such imaging methods suffer from inaccurate estimations of the distribution of the cells. Here, we show that single human breast cancer cells loaded with mesoporous silica nanoparticles concentrating the $^{68}$Ga radioisotope and injected in immunodeficient mice can be tracked in real time from the pattern of annihilation photons detected by positron emission tomography, with respect to anatomical landmarks derived from X-ray computed tomography. We show that the cells travelled at an average velocity of 50 mm/s and arrested in the lungs two-to-three seconds after tail-vein injection in the mice, which is consistent with the blood-flow rate. Single-cell tracking could be used to determine the kinetics of cell trafficking and arrest during the earliest phase of the metastatic cascade, the trafficking of immune cells during cancer immunotherapy, and the distribution of cells after transplantation.

## Abstract

One-sentence editorial summary:



*Corresponding author, pratx@stanford.edu.

Author contributions

KOJ performed *in vitro* and *in vivo* experiments. TJK performed physical tests and processed data. JHY characterized nanoparticles and optimized their radiolabelling. SR imaged *ex vivo* specimens. WZ reconstructed CT images. BH contributed to the design of the methods. GP reconstructed dynamic cell trajectory data. KOJ and GP designed the study and wrote the manuscript. KRH, SSG and GP supervised the study.

**Reporting summary**. Further information on research design is available in the Nature Research Reporting Summary linked to this article.

Competing interests

GP is listed as inventor on a US patent that covers the algorithm used in this study for cell trajectory reconstruction (US9962136B2). Other authors have no relevant conflicts of interest to disclose.

The travelling kinetics of single cells loaded with mesoporous silica nanoparticles concentrating the $^{68}$Ga radioisotope and injected in mice can be tracked in real time from the pattern of coincident gamma-rays detected by positron emission tomography.

*In vivo* molecular imaging tools are critically important to understand the role played by cell trafficking in physiological and pathological processes.[1] Metastasis, for instance, is the single most important factor for predicting cancer survival, and targeting the metastatic cascade could significantly improve clinical outcomes.[2] Other incurable diseases have seen unprecedented progress thanks to the development of cellular therapies,[3–5] which use stem cells or immune cells to target specific disease processes. In addition, many physiological processes such as haematopoiesis, immunity and embryonic development rely on the precisely orchestrated migration of cells throughout the body.[6,7]

While molecular imaging tools can be used to estimate distribution of cells non-invasively, the information they provide relates to population averages and not individual cells. Unfortunately, many biological properties of cells become lost once averaged in this manner, including specific migration routes and kinetics of individual cells. Intravital microscopy methods can interrogate single-cell processes *in vivo*, but not on the scale of the whole body, and only in shallow tissues.[8,9] A related approach, based on the photoacoustic effect, can visualize single red blood cells in the superficial vasculature of mice.[10] Additionally, magnetic resonance imaging (MRI) has demonstrated the capability to image single cells *in vivo*,[11,12] but only in uniform-background anatomical sites such as the brain and the liver, and without sufficient temporal resolution to track moving cells. Finally, an engineered bioluminescence reporter enzyme with 50-fold brighter emission was recently developed and used to optically visualize the arrest of single HeLa cells in the lungs of live mice.[13]

Positron emission tomography (PET) is the only non-invasive imaging modality capable of detecting picomolar probe concentration in humans. PET has been used for a variety of *in vivo* cell tracking applications[14–16] but, despite its exceptional sensitivity, its potential for single-cell imaging had not yet been demonstrated. The concept of tracking discrete particles using PET data originates from the field of chemical engineering, where the approach is used to estimate the dynamics of fluid and powder flows in complex opaque systems.[17] Recently, we developed a mathematical framework to extend this approach to the tracking of radiolabelled cells,[18] and validated the methodology experimentally using radioactive droplets.[19]

Here, we report the *in vivo* feasibility of “CellGPS”, a methodology for tracking the trafficking of single cells inside living subjects with exquisite sensitivity (Fig. 1). We use nanoparticles to efficiently ferry PET radioisotopes into live cells, then isolate single radiolabelled cells for injection into live mice. From the pattern of high-energy photons detected by PET, we infer, in real time, the position of these single cells with respect to anatomical landmarks derived from X-ray computed tomography (CT).

## Results

### Efficient method for cell radiolabelling

To radiolabel cells with high efficiency, we harness the exceptional cargo-carrying capacity of mesoporous silica nanoparticles (MSNs). Due to their large porous surface, these nanoparticles can efficiently transfer radionuclides into cells for real-time cell tracking applications. This study specifically considers $^{68}$Ga, a radiometal used for PET imaging of neuroendocrine tumours and metastatic prostate cancer. Despite is relatively short half-life (67 minutes), high-specific-activity $^{68}$Ga can be eluted from inexpensive $^{68}$Ge generators, making it an increasingly popular isotope for clinical applications.[20] Here, we show that MSNs are able to carry $^{68}$Ga into live cancer cells to achieve nearly 100 Bq per single cell, an amount of radioactivity sufficient for real-time tracking applications.[18,19] Although 100 Bq is truly a minute amount of radioactivity (it is less than 1 millionth of a standard PET dose), in terms of concentration, 100 Bq/cell is equivalent to 50 GBq/mL, which is 100 times higher than the concentration of $^{68}$Ga eluted from a medical generator. Nanoparticles are therefore essential to concentrate $^{68}$Ga into cells and achieve sufficient labelling.

MSNs were sourced from Sigma-Aldrich and physically characterized to reveal a spherical morphology with pore structure clearly visible on transmission electron micrographs (Fig. 2a). Hydrodynamic size distribution was estimated as 100-300 nm diameter (Supplementary Fig. 1a).

We then labelled these MSNs with $^{68}$Ga by exploiting the natural ability of MSNs to form stable coordination complexes with oxophilic radiometals through deprotonated Si-O− groups on their surface.[21] To optimize the method, MSNs were first labelled with stable $^{69}$Ga under various conditions and the products were analysed by electron microscopy (Supplementary Fig. 1b). Energy-dispersive spectroscopy was used to map the elemental composition of the labelled nanoparticles and show that $^{69}$Ga was uniformly distributed within the silica matrix (Fig. 2b). Other elements such as oxygen could be detected within the MSNs (Supplementary Fig. 1c).

The MSNs were then successfully labelled with clinical-grade $^{68}$Ga and purified to achieve >95% purity (thin-layer chromatography, Fig. 2c). Labelling efficiency, measured by gamma counting, was found to be as high as 0.5 Bq/nanoparticle. To further enhance cell loading, we fused $^{68}$Ga-labelled MSNs with a liposome-based transfection reagent,[22] coating their surface with a lipid bilayer (as confirmed by electron microscopy in Supplementary Fig. 1d).

Passive uptake of $^{68}$Ga-labelled MSNs was demonstrated in MDA-MB-231 breast cancer cells. The cells were incubated with $^{68}$Ga-labelled MSNs (~25 MBq/ml) for 40 min and washed three times. The entire labelling procedure took approximately 90 min (equivalent to 1.5 half-lives for $^{68}$Ga). The labelled cells were then imaged by electron microscopy to reveal endocytosis of the particles (Fig 2d and Supplementary Fig. 2a). The MSNs were further labelled using fluorescein isothiocyanate (FITC), and their uptake was verified by fluorescence microscopy (Fig. 2e) and quantified by flow cytometry (Fig. 2f). Higher cell uptake was observed for lipid-coated MSNs compared to uncoated MSNs (Supplementary

Fig. 2b). In quantitative terms, 95% of cells took up lipid-coated MSNs but only 20% took up uncoated MSNs (Supplementary Fig. 2c and Supplementary Fig. 2d).

Uptake of $^{68}$Ga-labelled MSNs by adherent MDA-MB-231 cells was confirmed by radioluminescence microscopy (RLM), a method with single-cell imaging resolution.[23] Areas of high radioactivity coincided with fluorescent nuclear staining (Hoechst 33342), indicating localization of radioactivity within cells (Fig. 2g). Cell labelling with $^{68}$Ga was more effective using lipid-coated MSNs than uncoated MSNs, and cells did not take up free $^{68}$Ga (Supplementary Fig. 3a). Furthermore, radiolabelling efficiency was relatively heterogeneous when analysed on a single-cell basis. A few cells presented no detectable signal (Supplementary Fig. 3b). Radiotracer efflux by cells reached 50% after two hours (gamma counting, Supplementary Fig. 4) and was composed primarily of free $^{68}$Ga radioisotope (thin-layer chromatography, Supplementary Fig. 5). Efflux is undesirable for cell tracking because it reduces the amount of radioactivity localized within the cells of interest while increasing background count rate due to redistribution of the radiotracer throughout the body.

Following these experiments, we characterized the viability and health of MDA-MB-231 cells following labelling with $^{68}$Ga-MSNs. Cell radiolabelling resulted in a small (5-15%) but significant ($P<0.001$) decrease in overall metabolic activity (WST-8 assay) for timepoints up to 24 h. At 48 h, no significant difference was detected (Fig. 2h). We then measured DNA damage in radiolabelled cells using the γH2AX assay. Cells treated with $^{68}$Ga-MSNs presented a substantial increase in the number of γH2AX foci, indicative of radiation-induced double-strand breaks (Supplementary Fig. 6). The level of DNA damage, while detectable, was significantly lower than that of cells exposed to an acute dose of X-ray radiation (Fig. 2i). Furthermore, it did not result in significant biological differences in apoptosis, proliferation and migration. We found no discernible difference in Annexin-V (apoptosis) staining between radiolabelled cells and controls (Supplementary Fig. 7), suggesting that exposure to $^{68}$Ga radiation is sublethal in these cells. Similarly, radiolabelling did not hinder cell proliferation (Ki-67 staining, Supplementary Fig. 8) and migration (wound healing assay; Supplementary Fig. 9). In conclusion, MDA-MB-231 cells maintained their essential functional characteristics after being labelled with $^{68}$Ga-MSNs. The small transient decrease in metabolic activity is likely due to temporary growth arrest while cells repair radiation damage. In addition, non-radioactive lipid-coated MSNs were well tolerated by cells and did not cause measurable changes in any of the biological endpoints. Finally, the labelling procedure can be applied to other cell types, such as 4T1 mouse mammary carcinoma, Raw 264.7 mouse macrophages, and adipose tissue-derived stem cells (ADSCs), with no significant differences in labelling efficiency or viability (Supplementary Fig. 10).

Imaging weakly radioactive sources, such as single cells, is challenging because most PET scanners contain naturally occurring radioactivity in their scintillation detectors.[24] Weak signals emitted by single cells can be drowned out by this intrinsic background. We optimized the acquisition protocol and raised the lower energy discrimination threshold to 425 keV to achieve an optimal trade-off between background noise and sensitivity (Supplementary Fig. 11). With these settings, an Inveon PET/CT scanner achieved a

background coincidence rate of ~ 2.6 counts/s, equivalent to 50-100 Bq randomly distributed throughout the field of view.

To demonstrate the ability of PET to image single cells, radiolabelled MDA-MB-231 cells were diluted and dispensed in Terasaki plates for enumeration (Fig. 2j). Wells containing 1, 2, 5, and 10 cells were identified by fluorescence microscopy and their contents were transferred to a standard 96-well plate for PET imaging. The images, which were reconstructed using standard 2D ordered-subset expectation maximization (OSEM) algorithm, showed increasing PET signal with increasing cell number (Fig. 2k). Importantly, a few single cells were clearly detectable by PET. Region-of-interest (ROI) analysis of the PET images confirmed the significant increase in signal intensity with increasing cell number (Supplementary Fig. 12). Additionally, we measured an average of 30 Bq/cell and a range of 0-110 Bq/cell using quantitative gamma counting (Fig. 2l). Finally, we estimated the limit of detection of PET by serially imaging a single cell (58 Bq) in a 5 cm water phantom. The cell was clearly visible in reconstructed images at 0, 45 and 70 min but not at 120 and 150 min (Supplementary Fig. 13a–b). These findings indicate that the limit of detection for CellGPS is below 28 Bq for conventional PET image reconstruction at the measured background count rate of 10 cps (Supplementary Fig. 13c).

## Static PET imaging of small cell populations in mice

To determine whether single cells could be imaged *in vivo*, approximately 100 MDA-MB-231 cells were labelled with $^{68}$Ga-MSNs (323 Bq in total) and DiO (fluorescent membrane dye), then injected intravenously into a mouse. The MDA-MB-231 cells line is derived from a pleural effusion of a patient with metastatic breast adenocarcinoma and is a common model of breast cancer metastasis to the lungs. PET/CT images, acquired immediately thereafter, showed diffuse signal in both lungs (Fig. 3a) and little detectable signal in other organs (Supplementary Fig. 14a). *Ex vivo* gamma counting confirmed significant radioactivity in the lungs compared with liver and spleen (Supplementary Fig. 14b). To confirm the arrest of the cells in the lungs, lung tissues were excised, and DiO-labelled cancer cells were visualized by fluorescence microscopy (Supplementary Fig. 14c & 14d). The arrest of cancer cells in the lungs was confirmed in another mouse injected with $10^6$ DiO-labelled cells (Supplementary Fig. 14e).

Other injection routes were also investigated. A bolus of ~10 radiolabelled cells (118 Bq in total) was injected in right thigh of a mouse and imaged with PET/CT images to reveal focal signal at the injection site (Fig. 3b), with no significant radioactivity elsewhere (Supplementary Fig. 15a). Similarly, ~10 cells were injected intraperitoneally in the abdomen (94 Bq; Supplementary Fig. 15b) and in the footpad (84 Bq; Supplementary Fig. 15c). In all cases, the PET signal was confined to the injection site.

Using the same workflow, we proceeded to image single cells in mice using PET. A set of radiolabelled single cells was isolated in Terasaki plates through limiting dilution. Then, using a portable radiation survey meter, we rapidly screened dozens of cells to find single cells with high radioactivity. Because cell uptake of $^{68}$Ga-MSN is variable, this screening process is critical to ensure that the selected cells have sufficient radioactivity for *in vivo* tracking.

In a first experiment, a single radiolabelled single cell (27 Bq) was injected into the footpad of a mouse. PET/CT images, acquired minutes after injection, depicted strong focal signal near the injection site (Fig. 3c) and no significant PET signal in other organs (Supplementary Fig. 15d). These images show that PET can image individual cells, which are much smaller than the resolution of the scanner. Indeed, the diameter of the PET signal was approximately 1.7 mm, which is consistent with the spatial resolution of the Inveon PET/CT scanner.

Next, isolated single cells (20-70 Bq) were injected via a butterfly catheter into the tail vein of mice ($n$=3). PET acquisitions were started either before ($n$=2) or after ($n$=1) single-cell injection. All injected mice presented a single locus of radiotracer accumulation in their lungs on PET/CT images (Fig. 3d). The major organs were then removed and imaged again *ex vivo* (Fig. 3e). Consistent with *in vivo* findings, focal uptake was observed in the lungs (Fig. 3f). *Ex vivo* gamma counting further measured 7-35 Bq in the lungs and less than 2 Bq in other organs (Fig. 3g). Finally, the lungs were dissected in an attempt to localize single arrested cancer cells. The tissue was chopped into five pieces; of these, only one contained significant radioactivity (Supplementary Fig. 16). We repeated this process until radioactive signal was confined to a piece of lung tissue smaller than 1 mm. We then imaged the tissue sample by widefield fluorescence microscopy and identified a single speck of enhanced red fluorescence (Fig. 3h). Finally, we imaged the area again by confocal microscopy and found a single locus positive for blue (Hoechst 33342) and red (DiI) fluorescence, which was due to pre-injection staining of the injected cell (Fig. 3i). Green fluorescence, imaged as a negative control, was negative for the identified locus.

To demonstrate that single cells can be imaged beyond the 67 min half-life of $^{68}$Ga, we tested the CellGPS workflow using $^{89}$Zr. We labelled MSNs with $^{89}$Zr using the same chelator-free method (2 h reaction time, Supplementary Fig. 17a), then transferred them into MDA-MB-231 cells (1 h incubation; Supplementary Fig. 17b & 17c). Efflux of $^{89}$Zr from cells was found comparable to that of $^{68}$Ga (during the first two hours) and did not exceed 50% even at 24 h (Supplementary Fig. 17d), confirming the stability of the radiochemical labelling. Finally, single cells labelled with $^{89}$Zr-MSNs (59 & 520 Bq/cell) were injected intravenously into mice ($n$=2) and imaged at multiple timepoints (0, 4, 24, and 48 h) using PET. Consistent with previous experiments, a single foci of uptake was detectable in the lungs (59 Bq/cell, Supplementary Fig. 18). The PET signal persisted up to 48 h and the cells did not move during that time. *Ex vivo* PET imaging confirmed the localization of the cells in the lungs. These results demonstrate that the CellGPS workflow can be used with long-lived radiometals to track single cells over different time scales. However, cells labelled with $^{89}$Zr suffered from measurable toxicity (13 days post-labelling) due to prolonged exposure to ionizing radiation (Supplementary Fig. 17e).

## Dynamic tracking of single cells in mice

Cell trafficking is a dynamic process. Real-time tracking could help shed light on the kinetics and migration routes of trafficking cells. Here, we demonstrate that PET data can be used to dynamically track the position of a single cell *in vivo*. By design, PET scanners record data in the list-mode format, a datafile that contains the attributes of every photon

coincidence event detected by the scanner, including time of detection, photon energy, and position of the detector elements involved. In the conventional PET workflow, list-mode data are binned into sinograms, then reconstructed to form tomographic images using an algorithm such as 2D-OSEM. In general, this approach does not permit dynamic tracking of single cells. Various particle tracking methods have been developed to estimate the time-varying position of a moving source directly the raw list-mode data, but their application has been limited to chemical engineering systems.[17] Our previous work modelled the trajectory of the cell as a cubic B-spline and computed its time-varying position by solving a convex optimization problem.[18]

The feasibility of tracking a moving cell was demonstrated first by enclosing a single radiolabelled MDA-MB-231 cell (36 Bq) into a 1.5 ml conical tube. Static PET/CT imaging detected a radioactive signal from the single cell inside the tube (Supplementary Fig. 19a). A list-mode acquisition was then performed, during which the tube was slowly moved along the axis of the scanner in one direction, then in the opposite direction, and finally removed from the scanner bore. The algorithm was able to compute the position of the object, even as it was being moved (Supplementary Fig. 19b). Furthermore, the count rate (Supplementary Fig. 19c) dropped (from 6.4 to 4.7 counts/s) once the vial had been removed from the scanner, suggesting that the cell contributed approximately 1.7 counts/s to the overall PET count rate, equivalent to 24 Bq (assuming 7% coincidence detection sensitivity).

To further validate this approach, we coiled a length of plastic tubing around a 3D-printed cylinder to form a helical test phantom (Fig. 4a). The phantom was placed in the bore of a PET scanner and a single MDA-MB-231 cell (67 Bq) was flowed at a speed of 1.36 mm/s through the tubing using a syringe pump. List-mode PET data were acquired for 10 min and then reconstructed into a 3D spline trajectory. Unlike the conventionally reconstructed image, which showed no localized signal (Supplementary Fig. 20a), the dynamically reconstructed trajectory matched the helical shape of the phantom, including its pitch and diameter (Fig. 4b). The single cell could also be seen exiting the scanner through the centre of the phantom (Supplementary Video. 1). We quantified the localization error (defined here as the root-mean square deviation from the ideal helical trajectory) and found it to be less than 5 mm (Supplementary Fig. 20b). Finally, we estimated the velocity of the cell according to its reconstructed trajectory (Fig. 4c). At its peak, the cell moved at the same speed as the injected bolus, although, at times, the cell slowed down significantly, possibly because it interacted with the walls of the plastic tubing. The code and data for this experiment are available online as an interactive code capsule (http://doi.org/10.24433/CO.5746631.v1).

We then applied this dynamic tracking methodology to single cells injected into live mice. First, the trajectories of static cells were reconstructed. Using the list-mode data from the previous footpad injection, we found that the single cell (27 Bq) remained at the injection site for the 10-min duration of the PET acquisition (Supplementary Fig. 21 and Supplementary Video. 2). For another mouse injected intravenously before the start of PET/CT acquisition, the radiolabelled cell (30 Bq) was correctly located in the mouse lung and no significant motion was observed during the 10 min acquisition (Supplementary Fig. 22 and Supplementary Video. 3), suggesting that the cell did not migrate after its arrest in

the lung. For these static cells, the 3D position reconstructed using the spline-based tracking algorithm was consistent with the PET images reconstructed through conventional OSEM.

Finally, real-time tracking was demonstrated by tracking a single cell (70 Bq) continuously, from its injection into the tail vein (via a catheter; Fig. 4d) to its arrest in the lungs. We monitored the arrival of the radiolabelled cell into the field of view of the scanner by plotting the rate of coincidence events as a function of time (Fig. 4e). Prior to the arrival of the cell, a count rate of 2 cps was measured from natural background radioactivity. Once the cell entered the bore of the scanner (at $t = 85$ s), the count rate jumped to 21 cps, and cell tracking was initiated. To visualize the pattern of coincident gamma ray detection, we charted the recorded coincidence events (shown as blue lines) and the reconstructed cell trajectory (yellow curved line) over a cross-sectional CT image of the mouse (Fig. 4f). The dynamic migration of the cell is also shown in Supplementary Video 4 and 5. According to the reconstructed trajectory, the single cell arrested in the lungs within 3 s of intravenous injection. The location of the arrested cell matched the focal signal seen on conventional PET/CT imaging (Supplementary Fig. 23a & 23b). The reconstructed cell migration route is also displayed as a transaxial view (Fig. 4g) and combined with a surface-rendered model of the mouse bony anatomy (Fig. 4h). An analysis of the reconstructed trajectory estimated the velocity of the cell at around 50 mm/s immediately post-injection (Supplementary Fig. 23c). For reference, the velocity of venous blood in the inferior vena cava in mice is approximately 40 mm/s, according to a previous MRI study.[25] Finally, as a control, PET data acquired from *ex vivo* organs were reconstructed. The algorithm localized the single cell to the excised lungs, and no motion was observed, apart from random fluctuations due to physical noise (root-mean-square error, RMSE <0.45 mm; Supplementary Fig. 23d and Supplementary Video 6).

## Discussion

One of the major findings of this study is that PET is sufficiently sensitive to image static single cells labelled with >20 Bq/cell $^{68}$Ga. This level of radioactivity was well tolerated by cells and didn't cause measurable changes in cell proliferation, migration and apoptosis. Standard 2D-OSEM reconstruction produced surprisingly good images of single cells *in vivo* after 10 min of acquisition with an optimized energy window that removes background noise. Labelled cells appeared in PET images as small hot spots (diameter ~1.7 mm) in an otherwise blank background. One advantage of tracking individual cells (as opposed to bulk populations) is that the presence of cells in an organ is less ambiguous because, unlike single cells, unbound tracer does not cluster to yield focal uptake. More advanced image reconstruction methods may provide advantages for single-cell imaging and should be investigated.

The second important finding of this study is that single migrating cells can be tracked dynamically directly from list-mode PET data. From a technical standpoint, dynamic cell tracking is vastly more challenging than static cell imaging, especially at high velocities. Our approach infers the position of the cell by fitting a 3D cubic B-spline to the dynamic pattern of gamma ray interactions recorded by the PET scanner. The method is flexible and can be tuned to maximize either spatial or temporal resolution, which are two competing

objectives. For instance, in Fig. 4 d–h, a single cell (70 Bq) was tracked from the tail vein to its arrest 3 s later in the lungs. During the first 5 s of tracking, the algorithm was tuned to be highly reactive to cell motion to accommodate the high velocity of the cell. Previous analyses indicate that robust tracking is achievable on the condition that the ratio of the cell velocity ($V$) to its activity ($A$) does not exceed 0.1 mm/s/Bq.[19] Physically, $V/A$ represents the average distance travelled by the cell between two radioactive decays. In this example, the initial velocity of the cell was estimated to be around 50 mm/s. Based on the $V/A$ criterion, a single-cell activity of 500 Bq—considerably higher than 70 Bq–would be required for accurate tracking. The reconstructed trajectory of the cell during the first 5 s of tracking should therefore be interpreted as qualitative rather than quantitative. Once the cell arrested in the lungs, the algorithm was adjusted to maximize localization accuracy. With these settings, the variability in the estimated position of the cell over time was ~ 0.4 mm RMSE, considerably better than the spatial resolution of the scanner. The phantom data (Fig. 4 a–c) also illustrate the importance of the $V/A$ criterion. In that experiment, a $V/A$ ratio of 0.02 mm/s/Bq was achieved, enabling robust tracking of the moving single cell.

This study also demonstrates the feasibility of tracking single cells over multiple days using $^{89}$Zr-MSNs. Serial PET imaging of single $^{89}$Zr-labelled cells revealed focal PET uptake in the lungs that was stable over two days. However, $^{89}$Zr lead to poor long-term cell viability due to its long half-life (Supplementary Fig. 17e). Most of the radiation damage is inflicted by positrons traveling through tissues at relativistic speeds. For single radiolabelled cells, it is important to note that only a tiny fraction of the total energy is deposited within the cell of interest. This is because emitted positrons have a physical range (in the case of $^{89}$Zr, 1.3 mm) that far exceeds the diameter of a typical cell. Yet, cells were still significantly affected by $^{89}$Zr labelling because of the slow decay of the radiolabel. Our results indicate that lower radioactivity should be used when tracking cells using $^{89}$Zr. From a purely theoretical perspective, a dose of 0.2 Bq/cell would generate 10 events after 10 min of PET acquisition (assuming a PET sensitivity of 10%). In the absence of background, ten events are sufficient to localize a static cell in 3D within a few millimetres of uncertainty. Thus, long-term tracking of cells using $^{89}$Zr may be possible, but it would require the development of PET scanners with high sensitivity and low intrinsic background. Additionally, radioprotectants may be used to further protect cells against radiation, by scavenging radiation-induced radicals and reactive oxygen species. For instance, compounds such as amifostine are used clinically in cancer patients to protect normal tissues against the acute effects of radiation therapy.[26]

While this study demonstrates the feasibility of tracking a single cell in a living subject, the behaviour of a heterogeneous cell population may not be well represented by a single cell. The CellGPS methodology could be extended to enable tracking of multiple cells simultaneously in the same subject. A previous study simultaneously tracked, *in vitro*, 16 yeast cells labelled with $^{18}$F-fluoride (32 Bq/cell). Individual cells were resolved and slow diffusion of the cells in the medium was observed.[27] An optimal transport regularization algorithm has also been investigated for tracking multiple single cells.[28] Tracking multiple cells will likely be possible provided that the following conditions are met: cells are separated from each other by at least 2-3 times the spatial resolution of the scanner; at any given time, no more than one cell moves rapidly within the imaged subject; and cells are

administered one-by-one such that they can be individually tracked from the injection site to the initial site of arrest. In the case of cellular therapies, where millions of cells are injected, it will be possible to label and track a small subset of cells using the CellGPS methodology.

Robust tracking of single cells using PET requires scanners with low background and high sensitivity. Preclinical PET scanners have much higher sensitivity than human-sized scanners because their bore almost completely surrounds the subject. However, almost all PET scanners suffer from non-negligible background noise arising from natural radioactivity within their lutetium oxyorthosilicate (LSO) detectors. Improved tracking performance can be achieved using PET detectors built from scintillator materials that do not contain significant radioactivity, such, for instance, bismuth germanate (BGO). In a previous study, we assessed that the amount of radioactivity required per cell for tracking could be reduced three-fold through the use of low-noise BGO detectors.[19]

Single cells may also be tracked using alternative labelling approaches. A previous study labelled yeast cells with $^{18}$F-fluoride by deleting fluoride export genes.[27] In addition, many small-molecule radiotracers are available to target proteins receptors and enzymatic processes, or bind to lipid membranes and other specific features of cells. These tracers may provide practical alternatives to nanoparticles and should be further investigated.

In conclusion, this study demonstrates the feasibility of tracking individual cells *in vivo*. Using the CellGPS methodology, we show that MDA-MB-231 cancer cells injected intravenously in mice arrest in the lung within 3 s of their injection after traveling at a velocity of up to 50 mm/s. The approach could have a number of significant applications in biology and medicine. For instance, it could be used to model and investigate the earliest stage of the metastatic cascade following intra-arterial administration of cancer cells. Pre-clinical studies have shown that hemodynamic forces, cell adhesion, blood flow, and biomechanical interactions play a pivotal role in the dissemination of cancer cells.[29] In addition, significant interest has emerged regarding the circulation of tumour cell clusters in the blood and their role in promoting metastasis formation.[30] Notably, cell clusters have slower dissemination kinetics than single cancer cells.[31] Other studies in zebrafish models have shown that cancer cells extravasate preferentially from smaller capillaries with slower blood flow.[32] However, cell migration studies are challenging to conduct in mammals for lack of suitable tools to track the migration kinetics of cells. CellGPS could be used in this context to develop a better understanding of how biomechanical forces and adhesion molecules influence the spread and kinetics of live cancer cells through the vasculature. In addition, cell velocity within blood vessels, measured *in vivo*, could be applied as a biomarker of cell adhesion molecules in the vascular bed. Beyond the study of cancer metastasis, CellGPS could be used to non-invasively measure routes and kinetics of immune cell mobilization in response to injury. Finally, the method could help support clinical trials of cancer immunotherapy and regenerative medicine. In recent years, PET scanners with extended field of view have been developed for total-body human PET imaging.[33] These highly sensitive systems could one day be used for translational applications involving tracking of single cells in humans.

# Methods

## Cell Line and Cell Culture

The MDA-MB-231 cell line (human invasive ductal carcinoma; obtained from Cell Biolabs in February 2016), Raw 264.7 mouse macrophages, and adipose tissue-derived stem cells (ADSCs; harvested from knee joints of Goettingen minipigs) were cultured in Dulbecco's Modified Eagle Medium (DMEM) medium (cat# 11885084, Thermo Fisher Scientific) with 584.0 mg/L of L-Glutamine and 1000.0 mg/L of D-Glucose. It was supplemented with 10% foetal bovine serum (FBS) and 1% antibiotic–antimycotic mix. 4T1 mouse mammary carcinoma cells were cultured in Roswell Park Memorial Institute (RPMI) 1640 medium (cat# 11875119, Thermo Fisher Scientific) with 300.0 mg/L of L-Glutamine and 2000.0 mg/L of D-Glucose. It was supplemented with 10% foetal bovine serum (FBS) and 1% antibiotic–antimycotic mix. These cells were cultured at 37°C and 5% CO2 in a humidified environment, up to a passage number of 20. ADSCs were only expanded up to passage 6.

## Physical Characterization of MSNs

Propylamine-functionalized mesoporous silica nanoparticles (cat# 749265-1G, Sigma-Aldrich) with 200 nm particle diameter and 4 nm pore size were physically characterized. The particles were deposited on 300-mesh carbon/formvar coated copper grids for imaging with a transmission electron microscope (JEM-1400 series 120kV, JEOL) equipped with a LaB6 emitter and a Gatan Orius 10.7-megapixel CCD camera. The elemental compositions of the MSNs after labelling with non-radioactive $^{69}$Ga was validated by energy-dispersive X-ray spectroscopy (EDS) and element mapping labelling using a transmission electron spectroscopy instrument (FEI Tecnai G2 3F20X-Twin microscope at 200 keV) equipped with a scanning TEM (STEM) unit with bright field/dark field detector, x-ray detector (EDS), and CCD camera. Finally, the concentration and hydrodynamic size distribution of the MSNs were determined by nanoparticle tracking analysis (NanoSight Ltd).

## MSN Radiolabelling with $^{68}$Ga

The MSNs were labelled with $^{68}$Ga using a chelator-free reaction method.[21] First, the nanoparticles were activated in ethanol overnight. Then, 4.5 μg of MSNs were added to a 1.5 ml tube containing 100 μl of MES buffer (0.1 M, pH 7.3). Subsequently, MSNs were labelled with $^{68}$Ga by adding 1.5 ml of $^{68}$GaCl3 solution (~600 MBq) eluted with HCl (0.1 N) from a clinical-grade generator. Some experiments used $^{68}$Ga from an older research generator. To maintain a reaction pH of 7.3, 30 μl of ammonium hydroxide solution (cat# 338818, Sigma-Aldrich) was added, and the mixture was incubated at 75°C for 15 min. The nanoparticles were then washed three times with PBS and centrifuged at 14,000 rpm for 1 min to remove residual $^{68}$Ga. To determine radiolabelling purity (% fraction of radioactivity bound to nanoparticles), the radiolabelled MSNs (1.5 μl) were deposited on a silica-gel impregnated iTLC-SG paper and 50 mM EDTA (pH 5) was used as the elution solvent. The samples were then analysed using a Bioscan AR-2000 radio-TLC plate reader (BioScan Inc).

### MSN Radiolabelling with $^{89}$Zr

To assess the feasibility of long-term cell tracking, the MSNs were labelled with $^{89}$Zr using the same reaction method.[21] First, the nanoparticles were activated in ethanol overnight. Then, 4.5 μg of MSNs were added to a 1.5 ml tube containing 1 ml of HEPES buffer (0.1 M). Subsequently, MSNs were labelled with $^{89}$Zr oxalic acid (shipped from the University of Alabama at Birmingham; 93 MBq in 100 μl). To maintain a reaction pH of 8–9, $Na_2CO_3$ solution (2 M) was added, and the mixture was incubated at 75°C for 2 h. The nanoparticles were then washed three times with PBS and centrifuged at 14,000 rpm for 1 min to remove residual $^{89}$Zr. To determine radiolabelling purity, the radiolabelled MSNs (1.5 μl) were deposited on a silica-gel impregnated iTLC-SG paper and 50 mM EDTA (pH 5) was used as the elution solvent. The samples were then analysed using a radio-TLC plate reader (AR-2000, BioScan Inc).

### Lipid Coating of MSN

To enhance MSN uptake in cells, a cationic liposome transfection agent (Lipofectamine 2000, cat# 11668030, Thermo Fisher Scientific) was also used to coat the surface of MSNs with a lipid bilayer. Two separate solutions were prepared: one containing a mixture of 4.5 μg of MSN and 500 μl of Opti-MEM (cat# 31985062, Thermo Fisher Scientific), and the other containing a mixture of 20 μl of Lipofectamine diluted in 500 μl of Opti-MEM. After 5 min of incubation at room temperature, the two solutions were combined and incubated for additional 15 min at room temperature. The coated MSNs were then recovered by centrifugation.

### Fluorescent Labelling of MSNs and Cells

The MSNs were labelled with FITC (fluorescein isothiocyanate isomer I, cat# 34321-M, Sigma-Aldrich) via formation of thiourea bond with NH2 functional groups on the MSN surface. Approximately 1 mg of MSNs were mixed with a solution of 1 ml FITC (0.1 mg/ml) and incubated at room temperature for 1 hr. The mixture was then washed three times with fresh PBS and centrifuged at 14,000 rpm for 1 min to remove excess FITC. For validation purpose, cells were labelled by incubation at 37°C for 15 min with fluorescent lipophilic tracers such as DiO (cat# V22886, Thermo Fisher Scientific, green fluorescence; Ex: 484 nm, Em: 501 nm) or DiI (cat# V22888, Thermo Fisher Scientific, red fluorescence; Ex: 565 nm, Em: 594 nm). Additionally, nuclear staining was performed by incubation with NucBlue Live ReadyProbes Reagent (a.k.a. Hoechst 33342, cat# R37605, Thermo Fisher Scientific) for 5 min at 37°C.

### Imaging and Flow cytometry of MSN Uptake in Cells

MDA-MB-231 cells ($2 \times 10^5$ cells/plate) were incubated with MSNs or lipid-coated MSNs (4.5 μg/mL) for 40 min. To characterize cell uptake of MSNs, the treated cells were fixed with 2% glutaraldehyde. The cells were subsequently deposited on 300-mesh carbon/formvar-coated copper grids and imaged by TEM as previously described. Similarly, the uptake of FITC-labelled MSNs was imaged by fluorescence microscopy (EVOS FL, ThermoFisher) and further quantified by flow cytometry (BD FACSAria Fusion sorter, BD Bioscience).

### Cell Viability Assay

MDA-MB-231 cells were seeded in 96-well plates ($2.5 \times 10^3$ cells/well). To evaluate the cytotoxicity of MSNs in cells, the viability cells was determined according to their metabolic activity at various time points, up to 48 h after treatment with 4.5 μg/mL of lipid-coated MSNs (with or without $^{68}$Ga labelling). The cells were incubated with CCK-8 (Cell Counting Kit-8) solution (cat# 96992, Sigma-Aldrich) and, after 1 h, mean optical density (OD) was measured at 450 nm using a GloMax multi-detection system (Promega). Blank measurements were acquired and subtracted.

### DNA Damage Assay (γH2AX Staining)

MDA-MB-231 cells ($1 \times 10^4$ cells/well) were seeded on a Lab-Tek II Chamber Slide (cat# 154453, ThermoFisher Scientific). After 24 h, cold MSNs and $^{68}$Ga-MSNs (4.5 μg/mL) were prepared and used to label the cells. As a positive control, MDA-MB-231 cells were treated to 3 Gy and 6 Gy of X-ray radiation (225 kVp; X-RAD SmART irradiator, Precision X-Ray Inc). One hour after completion of these procedures, the cells were fixed in 4% formaldehyde and stained with anti-phospho-histone H2A.X (Ser139) antibody (1:100; cat# 05-636, Sigma-Aldrich) overnight at 4°C. Secondary staining was performed using anti-mouse Alexa Fluor 488 antibody (1:100; cat# A-21202, ThermoFisher Scientific). Staining was imaged by fluorescence microscopy (EVOS FL; and DMi8, Leica Microsystems). Mean fluorescence intensity per cell was quantified using ImageJ software.

### Apoptosis Assay (Annexin-V Staining)

MDA-MB-231 cells ($1 \times 10^5$ cells/well) were seeded in 24-well plates. After 24 h, cold MSNs and $^{68}$Ga-MSNs (4.5 μg/mL) were prepared and used to label the cells. As a positive control, Olaparib (100 μM; cat# S1060, Selleck Chemicals) was used to treat the cells and induce apoptosis. Apoptosis was detected 48h after treatment using an Annexin-V staining kit (ab176749, Abcam, Cambridge, England). Fluorescence images were visualized using an EVOS FL Cell Imaging System. Fluorescence intensity was quantified by flow cytometry.

### Cell Proliferation Assay (Ki-67 Staining)

MDA-MB-231 cells ($1 \times 10^4$ cells/well) were seeded in Lab-Tek II Chamber SlideTM (cat# 154453, ThermoFisher Scientific). After 24 h, cold MSNs and $^{68}$Ga-MSNs (4.5 μg/mL) were prepared and used to label the cells. At 48 h after treatment, the cells were fixed in 4% formaldehyde and stained with anti-Ki67 antibody (1:100; ab15580, Abcam) overnight at 4°C. Secondary staining was performed using anti-rabbit Alexa Fluor 594 antibody (1:100; A-21442, ThermoFisher Scientific). Staining was imaged by fluorescence microscopy (EVOS FL) and quantified by flow cytometry.

### Cell Migration (Wound Healing Assay)

MDA-MB-231 cells ($5 \times 10^5$ cells/well) were seeded in 24-well plates and incubated in a $CO_2$ incubator for 24 h. After 24 h, cold MSNs and $^{68}$Ga-MSNs (4.5 μg/mL) were prepared and used to label the cells. Olaparib (100 μM) and enriched culture medium (30% FBS) were used as control conditions to respectively inhibit and promote cell migration. Using a pipette tip, the surface of the cell monolayer was scratched in a straight line. The migration

of the cells back into the area was then monitored by acquiring brightfield images at 0, 8, 24, and 48 h using an EVOS FL Cell Imaging System.

### Radioluminescence Microscopy of $^{68}$Ga-MSN uptake

A custom-built radioluminescence microscope (RLM) was used to image the uptake of $^{68}$Ga-labelled MSNs by cells. The construction and use of the microscope is described in a previous publication.[23] Prior to the experiment, MDA-MB-231 cells (2× $10^5$ cells) were seeded on a tissue-culture-treated 35 mm glass-bottom dish (cat# 81158, ibidi Labware GmbH) and incubated in a $CO_2$ incubator for 24 h. The cells were then treated with $^{68}$Ga-MSNs or lipid-coated $^{68}$Ga-MSN (~25 MBq/ml, suspended in 3 ml DMEM) for 40 min at 37°C. The cells were rinsed three times with PBS, then incubated with a nuclear fluorescent stain (Hoechst 33342) for 5 min at 37°C. To perform RLM imaging, a CdWO4 scintillator crystal (cat# CdWO4b101005S1, MTI Corp.) was placed on top of the radiolabelled cells. Fluorescence images were first captured using the DAPI channel (excitation/emission: 358 nm / 461 nm) to image the nuclei of adherent cells. RLM images were then acquired by setting the camera parameters to 1200 EM gain, 4×4 pixel binning, 150 ms exposure time, and 24,000 camera frames. Radioluminescence images were reconstructed using ORBIT (Optical Reconstruction of the Beta-ionization Track), a MATLAB toolbox developed in-house.[34] Radioactivity of each cell is expressed as counts per minute (cpm) and is calculated by enumerating the number of radioactive decays per cell throughout the hour-long acquisition. Radioactivity per cell was determined by region-of-interest analysis in MATLAB.

### Radioactivity Measurements using PET and Gamma Counter

Cells labelled with $^{68}$Ga-MSN were manually sorted into single cells through limiting dilution in Terasaki plates.[35] Fluorescence microscopy was used to enumerate the cells in each well. Wells containing 1, 2, 5, and 10 cells were identified, and their contents transferred to a 96-well plate for PET imaging (Inveon D-PET, Siemens Preclinical Solutions; 425-650 keV energy window, 10 min acquisition time). The radioactivity of single wells was assessed by region of interest (ROI) analysis using the Inveon Research Workplace (IRW) software. Another set of cells was prepared and measured by gamma counting (AMG, Hidex) with a counting time of 30 s per sample.

### Radiolabel Efflux

MDA-MB-231 cells (2 × $10^5$ cells) were seeded on tissue-culture-treated 35-mm glass-bottom dishes and incubated in a CO2 incubator for 24 h. The cells were then treated with lipid-coated MSNs (4.5 μg/mL) and $^{68}$Ga-MSNs (~25 MBq/ml, 3 ml in DMEM) for 40 min at 37°C, washed three times with PBS, incubated for another 30, 60, 90, or 120 min at 37°C, then washed again three times with PBS. Once all the cells had been washed, the radioactivity remaining in the samples was measured using gamma counting. To further determine the composition of the radioactive cell efflux, culture medium (1.5 μl) from $^{68}$Ga-MSN-treated cells was collected 2 h after labelling and deposited on a silica-gel-impregnated iTLC-SG paper, then EDTA (50 mM, pH 5) was used as the elution solvent. The samples were then analysed and compared to free $^{68}$Ga and $^{68}$Ga-MSN using a Bioscan AR-2000 radio-TLC plate reader.

### $^{68}$Ga-MSN Uptake and Viability for Various Cell Types

Four different types of cells—MDA-MB-231 human breast adenocarcinoma, 4T1 mouse mammary carcinoma, Raw 264.7 mouse macrophages, and ADSCs—were seeded ($2\times 10^5$ cells/group) on tissue-culture-treated 35-mm glass-bottom dishes. After 24 h, the cells were treated with unlabelled and $^{68}$Ga-labelled MSNs (4.5 μg/mL; 40 min incubation), then washed three times with PBS. After cell counting, radioactivity per 1,000 cells was measured using gamma counting. Cell viability was measured after incubating the cells with complete medium for 24 h and 48 h at 37°C (CCK-8 assay, cat# 96992, Sigma-Aldrich). Mean optical density (OD) was measured 1 h after adding the CCK-8 reagent at 450 nm using a GloMax multi-detection system.

### Single-Cell Limit of Detection

A 5 cm-diameter cylindrical phantom (Micro Hollow Sphere Phantom, Data Spectrum Corporation) was filled with water to simulate realistic photon scattering and attenuation. A single cell (58 Bq) labelled with $^{68}$Ga-MSN was placed in one of the hollow spheres, then the phantom was placed inside the bore of an Inveon D-PET scanner. Static PET images were acquired (425-650 keV energy window, 10 min acquisition) at various intervals (0, 45, 70, 120 and 150 min) to assess the limit of detection. The total number of counts was recorded. The list-mode data was reconstructed using both conventional OSEM and the CellGPS algorithm.

### *In Vivo* Cell Imaging using PET/CT

*In vivo* procedures were approved by the Administrative Panel on Laboratory Animal Care at Stanford University (protocol 28882) and followed animal-use guidelines and ethical regulations. Female athymic nude mice (6 weeks old; average weight of 20 g; strain# 490, Charles River) were used for *in vivo* studies. MDA-MB-231 cells were labelled with $^{68}$Ga-MSNs or $^{89}$Zr-MSNs, then different numbers of cells were injected into the animals through various routes, including intravenous, subcutaneous, intraperitoneal, and footpad injection. Radiolabelled single cells were screened using a portable radiation survey meter (Model 3 with GM detector, Ludlum), then loaded into a syringe. The volume of the injections was 100 μl. Mice were anesthetized during imaging using 1-2% isoflurane concentration and 0.5 L/min oxygen flow rate. After injection, static PET images were acquired (Inveon PET/CT; 425-650 keV energy window, 10 min acquisition). X-ray CT images were acquired using standard settings (80 kVp, 500 μA). Static PET images were reconstructed using conventional 2D-OSEM (4 iterations, 16 subsets, 0.8 mm pixel). Attenuation correction was performed using the CT data, and deadtime correction was applied based on a global estimate of the singles rate. No scatter correction was applied. Because a normalization scan was not available for the a custom 425-650 keV energy window used in this study, the reconstructed image data are given in relative machine units (shown in the colour bar). These values correspond to radioactivity concentration, up to an unknown multiplicative constant. Cells labelled with $^{89}$Zr-MSNs were imaged *in vivo* at various time points (0, 4, 24 and 48 h) using either an Inveon D-PET or GNEXT PET/CT scanner (SOFIE Biosciences). Anatomical reference was provided by acquiring either a transmission scan or a CT scan, according to the capability of the scanner.

### Dynamic Cell Tracking using PET/CT

A cylindrical phantom with helical grooves was 3D printed (Z18; MakerBot Industries), and PEEK tubing was wrapped along the grooves (51 mm diameter, 27 mm helical pitch). The phantom was placed inside the bore of an Inveon D-PET scanner. Using a syringe pump, a single radiolabelled single cell (67 Bq) was flown through the phantom at velocity of 1.36 mm/s while PET data were acquired (425-650 keV energy window, 10 min acquisition time). The list-mode data, which contained 2,165 coincidence events, was imported into MATLAB and the cell trajectory was reconstructed using our previously reported algorithm[18]. This reconstruction algorithm models the trajectory of the cell as a 3D cubic B-spline. The number of knots was set to have approximately 30 events per spline knot, which resulted in 72 knots (or 1 knot every 8.3 s). Scatter and background event rejection was achieved by establishing a distance threshold in the objective function of 7 mm. Cell trajectory data were plotted using MATLAB. For dynamic tracking in mice, a butterfly catheter was inserted into the mouse tail vein, and single radiolabelled cells were injected while PET data were acquired. The list-mode data file was imported into MATLAB and analysed to identify the time at which the cell entered the scanner. The spline knots were then defined to achieve a higher density of knots during the initial migration of the cell and a lower density of knots after its arrest. Spline knots were defined at T = 85, 86.3, 87.7 and 90 s initially, then every 23 seconds thereafter. This protocol allowed us to track the cell during its rapid migration while still achieving high tracking accuracy for the remainder of the scan. Given the high density of knots in the initial phase of the trajectory, the position of the cell is approximate and should be interpreted as a qualitative estimate (see Discussion).

### Ex *Vivo* Validation Studies

To identify the organs in which single cells have arrested, *ex vivo* tissues were imaged using PET (same parameters as for *in vivo* imaging) and radioactivity was measured using gamma counting. Whole lungs were cut into small chunks and individually measured with the gamma counter. Finally, the tissue chunks were imaged using a Zeiss SteREO Discovery V20 microscope and a Zeiss LSM-700 confocal microscope to confirm fluorescence of DiO/DiI-labelled cells in *ex vivo* tissues.

### Statistical Analysis

All data are presented as mean ± standard deviation. $P$ values < 0.05 were considered to be statistically significant and were obtained using Student's $t$-test (two-tailed, unpaired samples).

### Data availability

Raw PET/CT data (list-mode format) that support the findings of this study are available from the corresponding author upon request. All other data are available within the paper and its supplementary information files.

### Code availability

Computer codes used to reconstruct cell trajectories from list-mode PET data are provided as supplementary data and are also available as an online compute capsule (http://doi.org/10.24433/CO.5746631.v1).

## Supplementary Material

Refer to Web version on PubMed Central for supplementary material.

## References


1. Kircher MF, Gambhir SS & Grimm J Noninvasive cell-tracking methods. Nat. Rev. Clin. Oncol 8, 677–688 (2011). [PubMed: 21946842]
2. Eckhardt BL, Francis PA, Parker BS & Anderson RL Strategies for the discovery and development of therapies for metastatic breast cancer. Nat. Rev. Drug. Discov 11, 479–497 (2012). [PubMed: 22653217]
3. Dimmeler S, Burchfield J & Zeiher AM Cell-based therapy of myocardial infarction. Arter. Thromb. Vasc. Biol 28, 208–216 (2008).
4. Serup P, Madsen OD & Mandrup-Poulsen T Islet and stem cell transplantation for treating diabetes. BMJ. 322, 29–32 (2001). [PubMed: 11141151]
5. June CH, O'Connor RS, Kawalekar OU, Ghassemi S & Milone MC CAR T cell immunotherapy for human cancer. Science. 359, 1361–1365 (2018). [PubMed: 29567707]
6. Kupperman E, An S, Osborne N, Waldron S & Stainier DY A sphingosine-1-phosphate receptor regulates cell migration during vertebrate heart development. Nature. 406, 192 (2000). [PubMed: 10910360]
7. Wright DE, Wagers AJ, Gulati AP, Johnson FL & Weissman IL Physiological migration of hematopoietic stem and progenitor cells. Science. 294, 1933–1936 (2001). [PubMed: 11729320]
8. Lehr H-A, Leunig M, Menger MD, Nolte D & Messmer K Dorsal skinfold chamber technique for intravital microscopy in nude mice. Am. J. Pathol 143, 1055 (1993). [PubMed: 7692730]
9. Thurber GM, et al. Single-cell and subcellular pharmacokinetic imaging allows insight into drug action in vivo. Nat. Commun 4, 1504 (2013). [PubMed: 23422672]
10. Wang L, Maslov K & Wang LV Single-cell label-free photoacoustic flowoxigraphy in vivo. P. Natl. Aacad. Sci. USA. 110, 5759–5764 (2013).
11. Heyn C, et al. In vivo MRI of cancer cell fate at the single-cell level in a mouse model of breast cancer metastasis to the brain. Magn. Reason. Med 56, 1001–1010 (2006).
12. Hinds KA, et al. Highly efficient endosomal labeling of progenitor and stem cells with large magnetic particles allows magnetic resonance imaging of single cells. Blood. 102, 867–872 (2003). [PubMed: 12676779]
13. Iwano S, et al. Single-cell bioluminescence imaging of deep tissue in freely moving animals. Science. 359, 935–939 (2018). [PubMed: 29472486]
14. Adonai N, et al. Ex vivo cell labeling with 64Cu–pyruvaldehyde-bis(N4-methylthiosemicarbazone) for imaging cell trafficking in mice with positron-emission tomography. P. Natl. Aacad. Sci. USA. 99, 3030–3035 (2002).
15. Doyle B, et al. Dynamic tracking during intracoronary injection of 18F-FDG-labeled progenitor cell therapy for acute myocardial infarction. J. Nucl. Med 48, 1708–1714 (2007). [PubMed: 17909258]
16. Keu KV, et al. Reporter gene imaging of targeted T cell immunotherapy in recurrent glioma. Sci. Transl. Med 9, eaag2196 (2017). [PubMed: 28100832]
17. Parker D, Broadbent C, Fowles P, Hawkesworth M & McNeil P Positron emission particle tracking-a technique for studying flow within engineering equipment. Nucl. Instrum. Meth. A 326, 592–607 (1993).

18. Lee K, Kim TJ & Pratx G Single-Cell Tracking With PET Using a Novel Trajectory Reconstruction Algorithm. IEEE. Trans. Med. Imag 34, 994–1003 (2015).
19. Ouyang Y, Kim TJ & Pratx G Evaluation of a BGO-Based PET System for Single-Cell Tracking Performance by Simulation and Phantom Studies. Mol. Imag 15, 1536012116646489 (2016).
20. Fani M, Andre JP & Maecke HR 68Ga-PET: a powerful generator-based alternative to cyclotron-based PET radiopharmaceuticals. Contrast Media Mol. Imaging. 3, 53–63 (2008). [PubMed: 18383455]
21. Shaffer TM, et al. Silica nanoparticles as substrates for chelator-free labeling of oxophilic radioisotopes. Nano Lett. 15, 864–868 (2015). [PubMed: 25559467]
22. Liu J, Jiang X, Ashley C & Brinker CJ Electrostatically mediated liposome fusion and lipid exchange with a nanoparticle-supported bilayer for control of surface charge, drug containment, and delivery. J. Am. Chem. Soc 131, 7567–7569 (2009). [PubMed: 19445508]
23. Kim TJ, Turkcan S & Pratx G Modular low-light microscope for imaging cellular bioluminescence and radioluminescence. Nat. Protocols. 12, 1055–1076 (2017). [PubMed: 28426025]
24. Freedenberg MI, Badawi RD, Tarantal AF & Cherry SR Performance and limitations of positron emission tomography (PET) scanners for imaging very low activity sources. Phys. Medica 30, 104–110 (2014).
25. Kaul MG, et al. Magnetic particle imaging for in vivo blood flow velocity measurements in mice. Phys. Med. Biol 63, 064001 (2018). [PubMed: 29465412]
26. Andreassen CN, Grau C & Lindegaard JC Chemical radioprotection: a critical review of amifostine as a cytoprotector in radiotherapy. Semin. Radiat. Oncol 13, 62–72 (Elsevier, 2003). [PubMed: 12520465]
27. Langford ST, et al. Three-dimensional spatiotemporal tracking of fluorine-18 radiolabeled yeast cells via positron emission particle tracking. PLoS One. 12, e0180503 (2017). [PubMed: 28683074]
28. Schmitzer NS, KP; Wirth B. Dynamic Cell Imaging in PET with Optimal Transport Regularization. IEEE. Trans. Med. Imag 39, 1626–1635 (2020).
29. Wirtz D, Konstantopoulos K & Searson PC The physics of cancer: the role of physical interactions and mechanical forces in metastasis. Nat. Rev. Cancer. 11, 512 (2011). [PubMed: 21701513]
30. Aceto N, et al. Circulating tumor cell clusters are oligoclonal precursors of breast cancer metastasis. Cell. 158, 1110–1122 (2014). [PubMed: 25171411]
31. Choi JW, et al. Urokinase exerts antimetastatic effects by dissociating clusters of circulating tumor cells. Cancer Res. 75, 4474–4482 (2015). [PubMed: 26527605]
32. Follain G, et al. Hemodynamic forces tune the arrest, adhesion, and extravasation of circulating tumor cells. Dev. *Cell*. 45, 33–52. e12 (2018). [PubMed: 29634935]
33. Badawi RD, et al. First Human Imaging Studies with the EXPLORER Total-Body PET Scanner. J. Nucl. Med 60, 299–303 (2019). [PubMed: 30733314]
34. Yaron JR, Ziegler CP, Tran TH, Glenn HL & Meldrum DR A convenient, optimized pipeline for isolation, fluorescence microscopy and molecular analysis of live single cells. Biol. Proced. Online 16, 9 (2014). [PubMed: 24834016]
35. Nejadnik H, Castillo R & Daldrup-Link HE Magnetic resonance imaging and tracking of stem cells. Methods. Mol. Biol 1052, 167–176 (2013). [PubMed: 23743862]

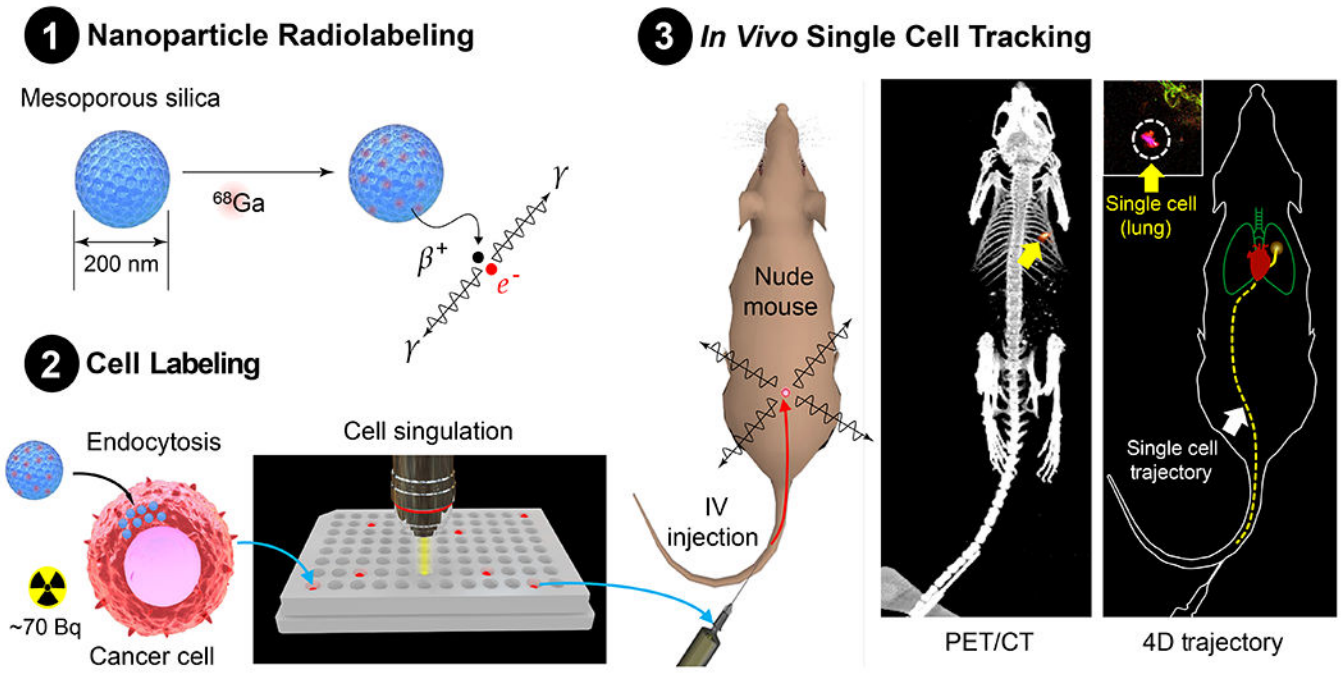


**Fig. 1 |. Overview of the CellGPS workflow.**

**a.** Mesoporous silica nanoparticles (MSNs) are used to concentrate $^{68}$Ga from a clinical PET generator. **b.** The nanoparticles are loaded to cells into achieve up to 100 Bq / cell (less than 1 millionth of a standard PET dose). **c.** Isolated single cells are administered into mice. Gamma rays emitted from single cells are captured by a small-animal PET scanner and processed by an algorithm to estimate the location of the moving cell in real time. In this example, single human breast cancer cells administered IV arrested in the lung, as confirmed by ex vivo dissection.

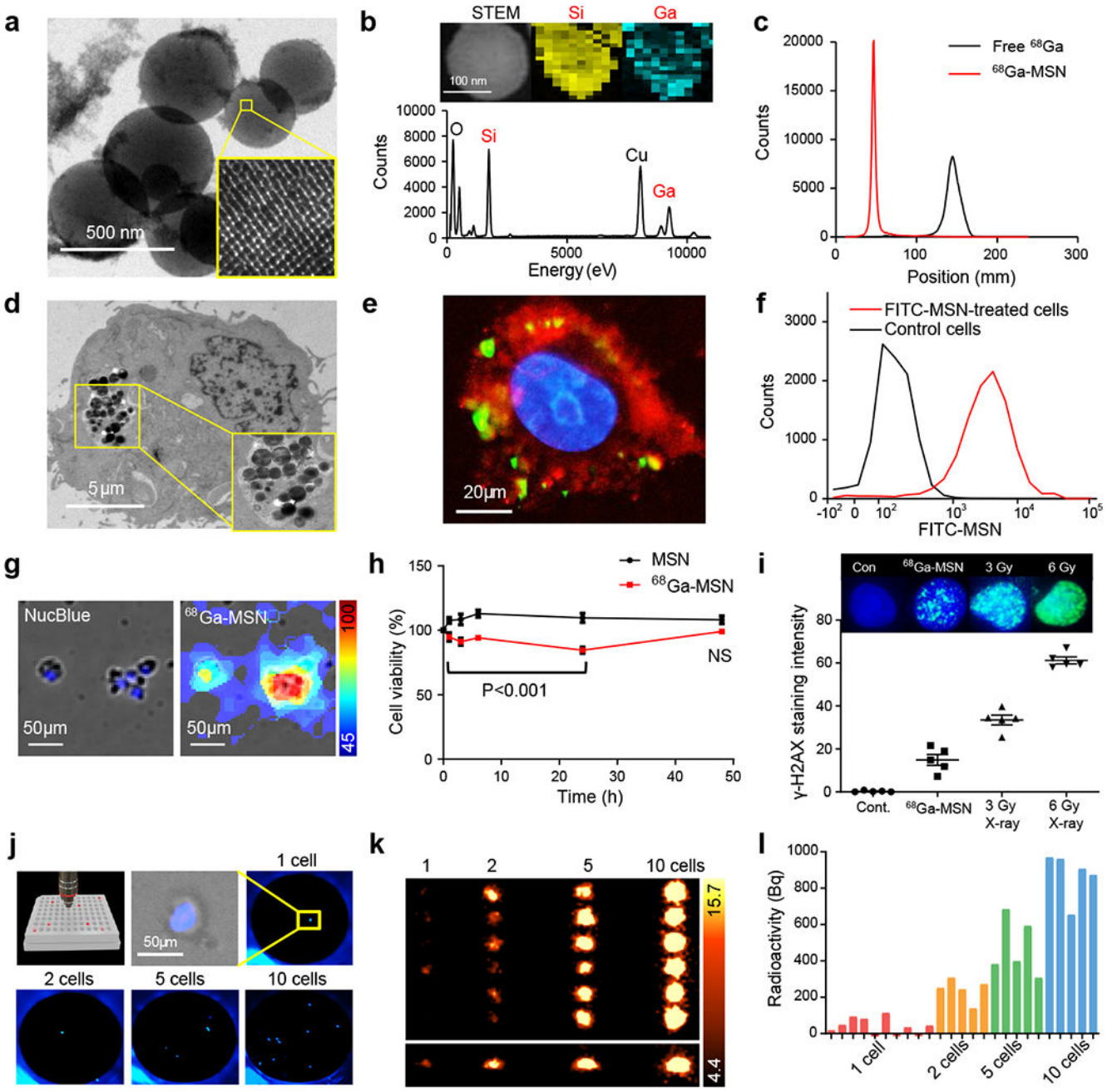


**Fig. 2 |. $^{68}$Ga-MSN labelling method for sensitive cell tracking.**

**a.** Transmission electron microscopy (TEM), showing MSN pore structure. **b.** Energy dispersive spectroscopy and elemental mapping of single MSN labelled with stable $^{69}$Ga. **c.** Radiochemical purity of $^{68}$Ga-MSN quantified using iTLC. **d.** TEM showing uptake of lipid-coated MSNs by MDA-MB-231 cell. **e.** Cellular uptake of FITC-labelled MSNs (green). Red highlights the cell membrane and blue the nucleus. **f.** Cell uptake of FITC-labelled MSN analysed by flow cytometry. **g.** Fluorescence (Hoechst 33342) and radioluminescence microscopy (RLM) of MDA-MB-231 cells following uptake of $^{68}$Ga-MSN. Colour bar shown as counts per pixel. **h.** Cell viability assay following treatment with

non-radioactive MSN and $^{68}$Ga-labelled MSN. Experiment performed in triplicate. The *P*-values (two-sided) were smaller than 0.001. NS, not significant. **i.** DNA damage measured as γH2AX staining (40 min after the end of the labelling procedure). **j.** Cell enumeration in Terasaki plates by fluorescence microscopy. **k.** PET imaging of various numbers of $^{68}$Ga-MSN-labelled cells (top: coronal view, bottom: sagittal view; colour scale shown as kBq/cc). **l.** Cell uptake (*in vitro* gamma counting) for different numbers of cells.

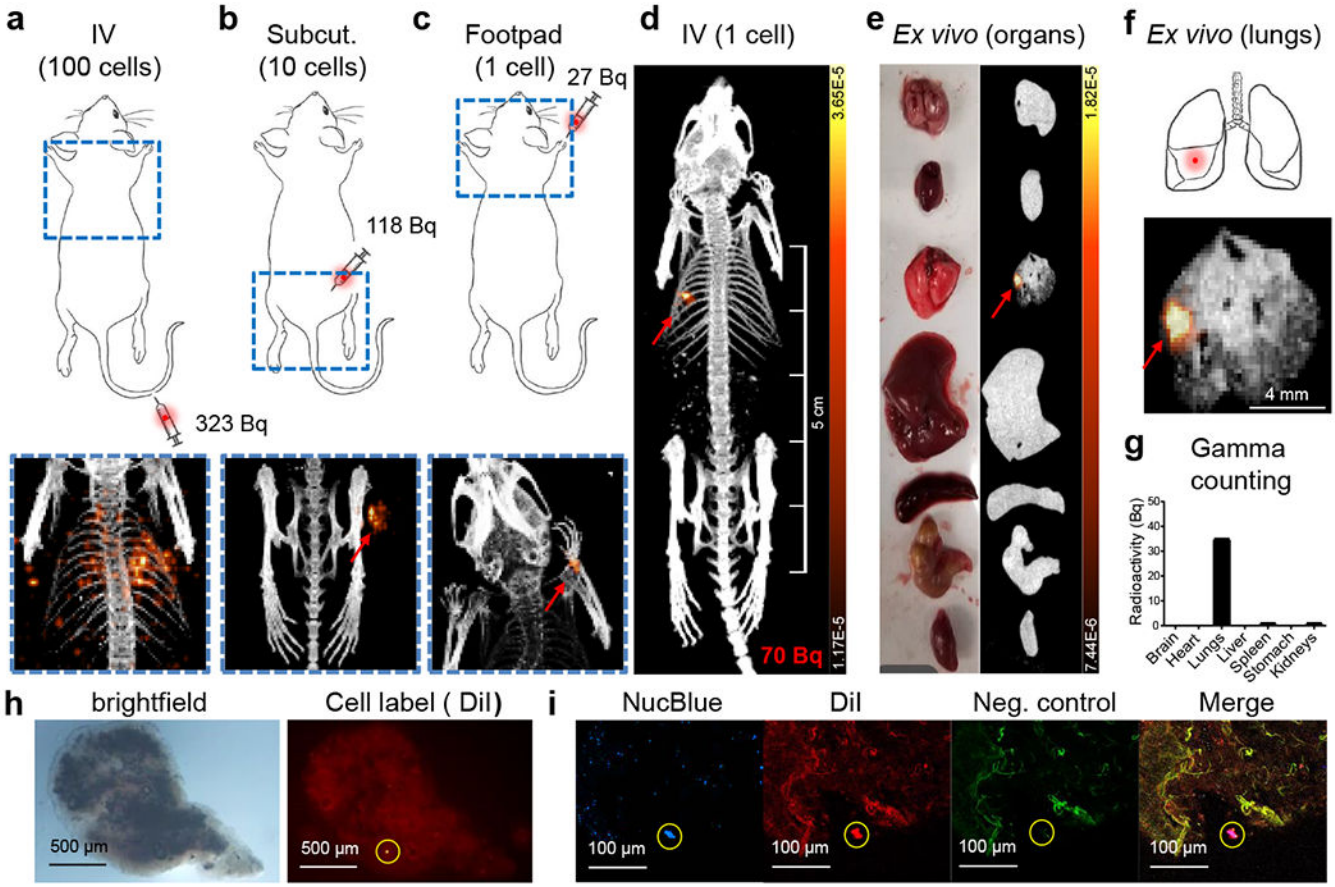


**Fig. 3 |. Static PET imaging of small cell populations in mice and *ex vivo* validation.**

**a.** MDA-MB-231 cells arrested in the lungs following IV injection of 100 radiolabelled cells. **b.** Visualization of a cluster of 10 cells after subcutaneous injection in the right thigh. **c.** Single radiolabelled cell detected after injection in the right forepaw. **d.** Single radiolabelled cell imaged after arrest in the left lung, following IV injection (experiment repeated three times). **e.** Photograph and PET/CT images of *ex vivo* organs from the same mouse (from top to bottom: brain, heart, lung, liver, spleen, stomach, kidney), and **f.** magnified view of the lungs. **g.** Gamma counting quantification of radioactivity in *ex vivo* organs. **h.** Brightfield and fluorescence imaging of *ex vivo* lung tissue highlights single locus with high DiI fluorescence. **i.** Confocal microscopy demonstrates dual staining for nucleus (Hoechst 33342, blue) and membrane (DiI, red) but no green fluorescence (negative control), confirming the localization in the lung of the injected cancer cell.

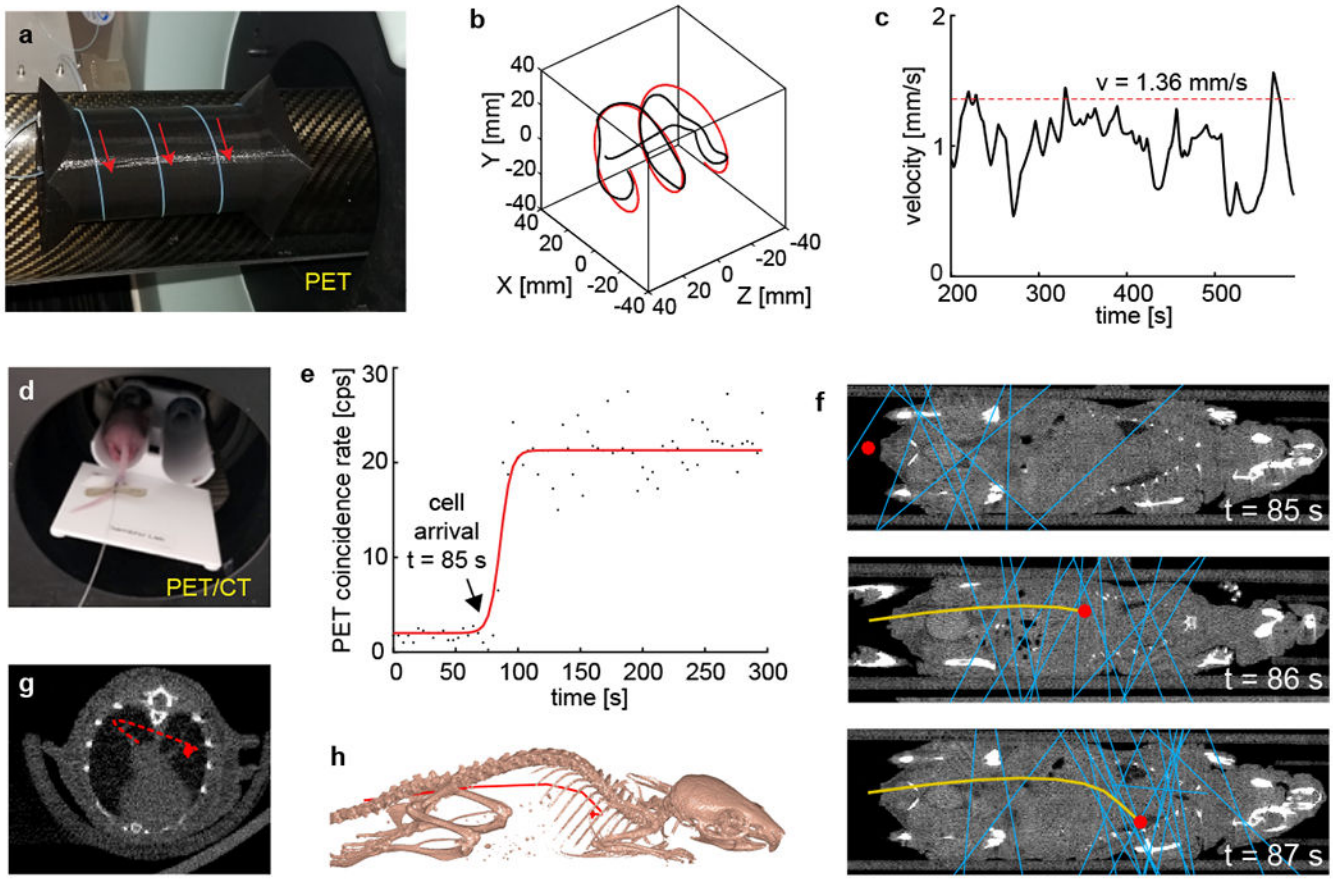


**Fig. 4 |. Dynamic PET tracking of single cells.**

**a.** A single radiolabelled cell is flowed through a length of tubing coiled around a 3D-printed cylinder. **b.** Cell trajectory reconstructed from list-mode PET data (black line) and closest helical fit (red line). **c.** Estimated cell velocity as a function of time (black line), and average velocity of the cell medium (dashed red line). **d.** Butterfly catheter inserted into mouse tail vein for simultaneous cell injection and PET imaging. **e.** Coincidence event rate recorded by the scanner. Events measured before cell arrival are due to background noise. **f.** Dynamic tracking of single cell in vivo, shown at three different time points. The blue lines represent coincidence events detected by the scanner. The red dot is the estimated location of the cell. The yellow line is the reconstructed trajectory. Coronal CT views are shown for anatomical reference. **g.** Reconstructed trajectory shown as a transaxial view, including cross-sectional CT slice through cell arrest location. **h.** Reconstructed trajectory shown with respect to 3D surface-rendered bony anatomy.